The Astrophysical Journal, 730:124 (15pp), 2011 April 1 doi:10.1088/0004-637X/730/2/124

THE THERMAL EVOLUTION OF ICES IN THE ENVIRONMENTS OF NEWLY FORMED STARS: THE CO_2 DIAGNOSTIC

A. M. Cook[1,5], D. C. B. Whittet[1], S. S. Shenoy[2,5], P. A. Gerakines[3], D. W. White[3], and J. E. Chiar[4]
[1] New York Center for Astrobiology and Department of Physics, Applied Physics & Astronomy, Rensselaer Polytechnic Institute, 110 Eighth Street, Troy, NY 12180, USA
[2] Spitzer Science Center, Mail Code 220-6, California Institute of Technology, Pasadena, CA 91125, USA
[3] Department of Physics, University of Alabama at Birmingham, 310 Campbell Hall, 1300 University Boulevard, Birmingham, AL 35294, USA
[4] SETI Institute, 189 Bernardo Avenue, Mountain View, CA 94043, USA
Received 2010 July 22; accepted 2011 February 4; published 2011 March 11

ABSTRACT

Archival data from the Infrared Spectrometer of the *Spitzer Space Telescope* are used to study the 15 μm absorption feature of solid CO_2 toward 28 young stellar objects (YSOs) of approximately solar mass. Fits to the absorption profile using laboratory spectra enable categorization according to the degree of thermal processing of the ice matrix that contains the CO_2. The majority of YSOs in our sample (20 out of 28) are found to be consistent with a combination of polar (H_2O-rich) and nonpolar (CO-rich) ices at low temperature; the remainder exhibit profile structure consistent with partial crystallization as the result of significant heating. Ice-phase column densities of CO_2 are determined and compared with those of other species. Lines of sight with crystallization signatures in their spectra are found to be systematically deficient in solid-phase CO, as expected if CO is being sublimated in regions where the ices are heated to crystallization temperatures. Significant variation is found in the CO_2 abundance with respect to both H_2O (the dominant ice constituent) and total dust column (quantified by the extinction, A_V). YSOs in our sample display typically higher CO_2 concentrations (independent of evidence for thermal processing) in comparison to quiescent regions of the prototypical cold molecular cloud. This suggests that enhanced CO_2 production is driven by photochemical reactions in proximity to some YSOs, and that photoprocessing and thermal processing may occur independently.

Key words: astrochemistry – dust, extinction – evolution – infrared: ISM – ISM: molecules – stars: pre-main sequence

Online-only material: color figures

1. INTRODUCTION

Icy material is the dominant carrier of the CNO group of chemical elements from interstellar clouds to protoplanetary disks. Understanding the nature and evolution of this material is thus an important astrophysical and astrobiological goal, with significance for models of interstellar chemistry, planet formation, and the origin of comets and other icy bodies in the solar system. The absorption feature identified with the bending mode of solid carbon dioxide (CO_2) near 15 μm has proven to be particularly useful in this regard, providing insight into the thermal evolution as well as the composition of the ices. Absorption at this wavelength is widely observed in spectra obtained with the *Infrared Space Observatory* (*ISO*) and the *Spitzer Space Telescope* for lines of sight that contain substantial columns of cold interstellar dust and molecular gas in our Galaxy. Detections have been made toward both dust-embedded young stellar objects (YSOs; Gerakines et al. 1999; Gibb et al. 2000, 2004; Nummelin et al. 2001; Boogert et al. 2004; Watson et al. 2004; Pontoppidan et al. 2005, 2008; Zasowski et al. 2009) and background field stars located behind dense molecular clouds (Bergin et al. 2005; Knez et al. 2005; Whittet et al. 2007, 2009). These studies demonstrate that CO_2 is a ubiquitous component of the ices that reside upon dust grains inside the clouds. It is, indeed, expected that CO_2 will form efficiently in the environments of YSOs, where a source of activation energy needed to drive reactions such as $CO + O \rightarrow CO_2$ and $CO + OH \rightarrow CO_2 + H$ is readily available. Laboratory experiments demonstrate, for example, that CO_2 is produced when ice mixtures containing H_2O and CO are subjected to UV radiation in conditions analogous to those in a molecular cloud near a hot embedded star (e.g., d'Hendecourt et al. 1986). However, the presence of CO_2 in lines of sight toward background field stars shows that CO_2 is also formed in quiescent regions of molecular clouds that lack a local energy source, presumably by grain surface reactions that proceed at very low temperature (e.g., Whittet et al. 1998; Langer et al. 2000; Pontoppidan et al. 2008). Recent laboratory work demonstrates the formation of CO_2 from CO and OH at temperatures as low as 10 K (Oba et al. 2010).

Since YSOs are born in regions that were once quiescent, observations of field stars provide insight into initial conditions prior to thermal and/or photochemical evolution driven by star formation. The observations show that ices in quiescent clouds are composed primarily of three species, H_2O, CO, and CO_2, of which only CO is present in concentrations consistent with adsorption of molecules formed in the gas phase. At intermediate densities, the most abundant reactive species attaching to grain surfaces are H, O, and CO, from which H_2O and CO_2 appear to form in tandem by hydrogenation of O and oxidation of CO to produce a "polar" (H_2O-dominated) ice layer. In regions of higher density where almost all of the gaseous hydrogen is molecular, a relatively H-poor "nonpolar" ice layer accumulates, dominated by CO accreted directly from the gas. Other potential constituents such as methanol (CH_3OH) and CN-bearing species are sometimes abundant in the spectra of YSOs but have low concentrations in the

[5] Current address: NASA Ames Research Center, Mail Stop 245-6, Moffett Field, CA 94035, USA.

molecular-cloud ices (e.g., Boogert et al. 2008; Gibb et al. 2004, and references therein), suggesting that photochemical or thermally driven reactions are needed for their efficient production. CO_2 and CH_3OH compete for the available CO in reaction networks based on surface chemistry: CH_3OH forms by successive hydrogenation reactions in the sequence $CO \rightarrow HCO \rightarrow H_2CO \rightarrow H_2COH \rightarrow CH_3OH$, of which the first and third possess activation energy barriers (Cuppen et al. 2009). Whereas CH_3OH can readily undergo further processing to form more complex organic species, the more stable CO_2 is something of a bottleneck (Langer et al. 2000). In initiating CH_3OH production, the energy released by newly born stars may thus be vital in driving chemical evolution toward greater complexity. The resulting increase in the mobility of species in the solid may also lead to physical changes such as segregation and crystallization. Ultimately, heating may result in partial or complete sublimation of the ices, and the molecules thus released may then undergo further evolution in the gas phase in hot cores or corinos around the YSO (e.g., Herbst & van Dishoeck 2009).

The importance of the CO_2 bending mode as a diagnostic signature of the composition and thermal environment of the ice mixture in which the CO_2 resides was demonstrated by extensive work on laboratory analogs (Ehrenfreund et al. 1998, 1999; Dartois et al. 1999; van Broekhuizen et al. 2006; White et al. 2009). The profile shape of the 15 μm absorption feature is sensitive to the molecular environment of the CO_2, enabling discrimination between CO_2 in polar (H_2O-dominated) and nonpolar (CO-dominated) phases at low temperature, and providing evidence for formation and segregation of linked CO_2–CH_3OH molecular groups when the ices are heated. Dilute CO_2-bearing amorphous ice mixtures that display smooth profiles at low temperature evolve upon heating to display subfeatures characteristic of irreversible changes as the ice begins to crystallize above 50–60 K in laboratory-based experiments (e.g., White et al. 2009). Observations with *ISO* and with *Spitzer* have demonstrated that these subfeatures are present in the spectra of many YSOs, and are (as expected) lacking in the spectra of unprocessed ices seen toward background field stars (e.g., Gerakines et al. 1999; Watson et al. 2004; Pontoppidan et al. 2008; Whittet et al. 2009).

Our group and others have developed techniques for fitting observed ice profiles with models based on laboratory spectra for interstellar analogs. In general, the observed CO_2 bending-mode profile is not well matched by a single CO_2-bearing ice mixture, but it can be modeled satisfactorily by a combination of two or more mixtures, of which one is H_2O-rich (representing the polar ice component described above) and the others are typically H_2O-poor. Results for unprocessed ices observed in field-star spectra are well matched by a superposition of polar and nonpolar mixtures at low temperature ($\lesssim$ 20 K; Bergin et al. 2005; Whittet et al. 2007, 2009). Observed variations in the CO_2/H_2O abundance ratio between three different molecular clouds were shown to have little to no impact on the 15 μm CO_2 profile, indicating that a robust benchmark has been established for comparison with regions in which the ices are exposed to harsher conditions.

The present paper extends our previous work on the field stars to encompass the rich legacy of *Spitzer* spectra available for low-mass YSOs (Section 2). The data are compared with the extensive library of spectra for interstellar ice analogs now available from the databases of the Astrophysics Laboratories of Leiden University (Ehrenfreund et al. 1997, 1999) and the University of Alabama at Birmingham (UAB; White et al. 2009), spanning a wide range of temperature (5–150 K) as well as composition. A least-squares procedure is used (Section 3) to fit each observed profile with an appropriate combination of laboratory analogs, allowing the general properties of the ices to be characterized. The spectra are also used to determine the solid CO_2 column density, $N(CO_2)$, in each line of sight, and to investigate the correlation of $N(CO_2)$ with extinction (Section 4), with the column densities of other species in the ices, and with characteristics of the YSOs such as spectral index and the presence or absence of structure in the observed CO_2 profile (Section 5). The set $\{H_2O, CO, CO_2\}$ contains the dominant quantifiable components of interstellar and preplanetary ices in most lines of sight, and we combine new and previously published results to investigate the intercorrelation of these three species with the aid of ternary plots (Section 5.3). Our conclusions are summarized in the final section.

2. OBSERVATIONS

2.1. Source Selection

Sources were chosen on the basis of known YSO status (using the SIMBAD database and references therein as a guide) with clear detections of the 15 μm CO_2 ice feature in spectra from the short-high (SH) module of the *Spitzer* Infrared Spectrometer (IRS; Houck et al. 2004). Only sources exhibiting absorption profiles deemed to have sufficient depth and signal-to-noise ratio for reliable modeling were selected. The final list (Table 1) includes six sources observed as part of our Cycle 1 *Spitzer* program targeting the Taurus and Ophiuchus Molecular Clouds (PID 3303; Principal Investigator: D. Whittet), namely, MHO-3, IRAS 04154+2823, V410 X-ray 2, IRAS 04181+2654, ITG 25B, and Oph 125; these were supplemented by a further 22 sources in various star-forming regions, taken from the *Spitzer* data archive. CO_2 spectra for most of these additional sources have been published previously by Pontoppidan et al. (2008). Note, however, that we adopt a somewhat different strategy for laboratory fitting compared with these authors, as detailed in Section 3.2 below.

2.2. Data Acquisition and Reduction

All observations reported here were obtained with the SH module of the *Spitzer* IRS, which covers the wavelength range 10–19.5 μm at a resolving power $\lambda/\Delta\lambda \sim 600$ (Houck et al. 2004). Astronomical Observation Request (AOR) keys, which provide unique identification of each spectrum in the *Spitzer* archive, are listed in Table 1. Most of the observations were carried out in the staring mode of the IRS; however, the library of suitable spectra was extended by searching the *Spitzer* archive for observations of sufficient quality made in spectral mapping mode. Results for five objects in our sample are based on mapping-mode observations (L1489 IR, DF Tau, L1551 IRS5, TMC-1A, and Elias 18). Each spectrum was processed with the *Spitzer* Science Center pipeline version S14.0.0, which provided basic calibration data. The spectra were reduced using the c2d pipeline, which offers a reasonable estimate of the background for subtraction from sources with deep absorption features. See Pontoppidan et al. (2008) for further details of this pipeline.

2.3. Continuum Fitting

The flux continuum for each source was determined by low-order polynomial fitting. In addition to the CO_2 feature, many

Table 1
Summary of Observations

Source Name	IRAS Association	Other Association	Region	R.A. (J2000) (h m s)	Decl. (J2000) (° ′ ″)	AOR Key	Date Observed	Program ID
HH 14	IRAS 03254+3050		Lynds 1450	03 28 34.51	+31 00 51.2	11827200	2005 Feb 9	172
B1 IRS	IRAS 03301+3057	Pers Emb 2	Barnard 1	03 33 16.67	+31 07 55.0	15918080	2005 Sep 9	179
B5 IRS3	IRAS 03439+3233		Barnard 5	03 47 05.81	+32 43 09.0	5635072	2004 Sep 29	172
B5 IRS1	IRAS 03445+3242	HH366	Barnard 5	03 47 41.61	+32 51 43.8	5635328	2004 Feb 4	172
L1489 IR	IRAS 04016+2610	HH360	Taurus	04 04 43.07	+26 18 56.4	3528960	2004 Feb 8	2
MHO-3	IRAS 04114+2757		Taurus	04 14 30.55	+28 05 14.6	10717440	2005 Feb 9	3303
IRAS 04154+2823	IRAS 04154+2823		Taurus	04 18 32.03	+28 31 15.4	10718208	2004 Sep 30	3303
V410 X-ray 2			Taurus	04 18 34.44	+28 30 30.2	10718464	2005 Feb 8	3303
IRAS 04181+2654	IRAS 04181+2654		Taurus	04 21 11.46	+27 01 09.4	10719488	2004 Oct 4	3303
DG Tau B			Taurus	04 27 02.66	+26 05 30.5	3540992	2004 Feb 8	2
DF Tau	IRAS 04239+2535		Taurus	04 27 02.80	+25 42 22.3	3530752	2004 Feb 8	2
L1551 IRS5	IRAS 04287+1801		Lynds 1551	04 31 34.08	+18 08 04.9	3531776	2004 Mar 5	2
TMC-1A	IRAS 04365+2535		Taurus	04 39 35.19	+25 41 44.7	3533312	2004 Feb 28	2
Elias 18	IRAS 04369+2539	Ced 38, IC 2087	Taurus	04 39 55.74	+25 45 02.0	3533312	2004 Feb 28	2
ITG 25B	IRAS 04370+2559		Taurus	04 40 08.00	+26 05 25.4	10722560	2004 Oct 4	3303
HH 47 IR	IRAS 08242−5050		HH 46/47	08 25 43.78	−51 00 35.6	5638912	2003 Dec 15	172
Ced 110 IRS6	IRAS 11057−7706		Chameleon I	11 07 09.23	−77 23 04.3	5639680	2004 Sep 1	172
Cha II-28	IRAS 12553−7651		Chameleon II	12 59 06.63	−77 07 40.0	9830912	2005 Mar 12	179
CG 12	IRAS 13546−3941		DC 316.5+21.2	13 57 38.94	−39 56 00.2	5642752	2004 Jul 17	172
B228	IRAS 15398−3359		Barnard 228	15 43 02.26	−34 09 06.7	5828864	2005 Sep 9	179
Oph 125		IRS 37, [GY92] 246	Ophiuchus	16 27 18.17	−24 28 52.6	10727168	2005 Mar 18	3303
CRBR 2422.8-3423			Ophiuchus	16 27 24.61	−24 41 03.3	9346048	2004 Mar 26	172
IRS 63	IRAS 16285−2355		Ophiuchus	16 31 35.53	−24 01 28.3	12676608	2006 Mar 21	2
CK 1		EC 90	Serpens	18 29 57.75	+01 14 05.9	9828352	2004 Sep 2	172
R CrA IRS5			Corona Australis	19 01 48.03	−36 57 21.6	9835264	2005 Apr 15	179
R CrA IRS7a		[B87] 10	Corona Australis	19 01 55.32	−36 57 22.0	9835008	2005 Apr 15	179
L723	IRAS 19156+1906		Lynds 723	19 17 53.16	+19 12 16.6	14905856	2005 Oct 14	20604
L1262	IRAS 23238+7401		Lynds 1262	23 25 46.70	+74 17 37.2	9833728	2004 Oct 24	179

sources exhibit a substantial absorption at shorter wavelengths, attributed to the wing of the broad 10 μm interstellar silicate feature blended with the weaker libration mode of H_2O-ice. To eliminate this contribution, some spectra required separate continuum fits on each side of the 15.2 μm profile. Figure 1 shows L1489IR and TMC-1A as examples of "normal" and "composite" continuum fits, respectively. In the case of L1489IR, a single fit over the entire SH spectrum, excluding the 14.7–15.9 μm segment containing the CO_2 feature, was found to be satisfactory. In the case of TMC-1A, a fit to the continuum at shorter wavelengths (from 10 to 14.5 μm) was combined with a fit to the segments 14.5–14.8 μm and 15.9–19.5 μm at longer wavelengths. Including some of the points on the short-wavelength side of the CO_2 feature allowed us to create a smooth continuum transition over the absorption band. The optical depth spectrum was then calculated routinely for each source from the ratio of the continuum to the observed flux, i.e., $\tau(\lambda) = \ln[F_{\rm cont}(\lambda)/F_{\rm obs}(\lambda)]$. The contribution of uncertainties in continuum fits to errors in column density estimates (Section 5) are small (typically a few percent) and no greater than the statistical errors in the data in each case.

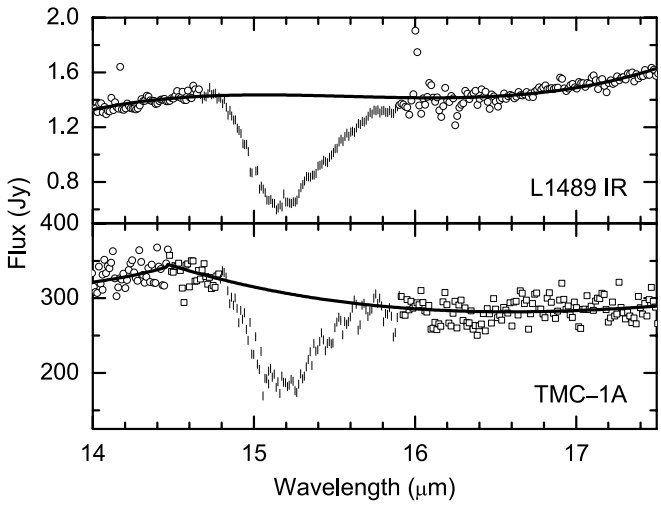

Figure 1. Examples of local continuum fitting. Vertical hatches are data points within the absorption profiles not included in the fits. L1489IR (top panel) illustrates the fitting method used for the majority of our spectra, where only a single polynomial fit to the continuum data points (represented by circles) was required. The fit to TMC-1A (bottom panel) utilizes two intersecting polynomials, one fit to the circles and one to the squares. See the text (Section 2.3) for details.

3. FITTING THE CO_2 PROFILE

3.1. Laboratory Databases

Astrochemical laboratories are a necessary and influential resource for infrared astronomy. As noted in Section 1, spectra for a wide range of specific ice mixtures are available for use in fitting astronomical spectra obtained from infrared observations. To fit the *Spitzer* CO_2 spectra, we utilized the databases available from the Astrophysical Ice Laboratory at Leiden University[6] and the Astrophysics Laboratory at the UAB.[7] These groups have created and characterized ice mixtures with a range of compositions and exposed to a range of temperatures, resulting

[6] Ehrenfreund et al. (1997, 1999); see http://www.strw.leidenuniv.nl/~lab.
[7] White et al. (2009); see http://www.phy.uab.edu/labastro/databases.html.

in libraries that contain a total of 1381 spectra relevant to this project, all of which are public or available upon request. The fitting routine draws fit components from this suite of spectra, as described below (Section 3.2).

Realistic simulations of interstellar spectra calculated from laboratory spectra must take particle size and shape effects into consideration. These effects have been found to have significant impact on the structure of strong absorption features at shorter infrared wavelengths (e.g., Tielens et al. 1991; Ehrenfreund et al. 1997), including the 4.1μm stretching-mode feature of CO_2 (e.g., Gerakines et al. 1999). At the wavelength of the CO_2 bending mode, however, the grains are most likely well into the Rayleigh limit, i.e., $2\pi a \ll 15$ μm, where a is the radius of the largest grains (Pontoppidan et al. 2008): in this situation, grain size and shape effects typically have negligible influence on profile shape. They are also less important for the relatively broad ice features seen in polar mixtures, in comparison to the sharply peaked features of *pure* CO_2 ices (Ehrenfreund et al. 1997 and references therein; note that pure CO_2 ices were not used in any of our fits). Moreover, optical constants used to calculate grain size and shape corrections are controversial (e.g., Boogert 1999; Moore et al. 2010) and can introduce widely varying results according to assumptions made. In view of these considerations, we have chosen to omit grain shape corrections from the laboratory spectra used in the current work. All of our astronomical spectra are well fit by uncorrected laboratory data, and the fits are interpreted primarily as a qualitative description of the ice components toward different lines of sight.

3.2. Fitting Procedure

The *Spitzer* optical depth spectra were input to a fitting routine developed by Gerakines et al. (1999), similar to that used by Chiar et al. (1995). The routine determines the best fit to each spectrum via χ^2_ν (reduced chi-squared) minimization. The fitting procedure assumes that the profile can be modeled by a combination of two distinct ice components, as in our previous work: this choice is justified as the smallest number of components capable of giving an acceptable fit, but it should be noted that deconvolution into as many as five components has been used to fit CO_2 bending-mode profiles in some previous work.[8] Uniqueness is naturally an important issue, and we adopt the strategy that is preferable to use only as many components as will make a good fit. In reality, most fitting routines do not provide "unique" fits; often, several combinations of ices will provide acceptable fits (with similar χ^2_ν residuals) to a given observed spectrum. Our aim is to obtain a "family" of fits that are similar in character (i.e., with comparable ratios of polar to nonpolar ices or crystalline ices at similar temperatures), with as few components as deemed necessary, based on observation. This procedure enables the general nature of the ices in a given line of sight to be characterized.

The ices in the laboratory database were divided into four groups: (1) 21 polar ices[9] at temperatures below 60 K, (2) 33 nonpolar ices at temperatures below 30 K, (3) 22 polar ices with no methanol constituent at temperatures above 60 K, and (4) 954 ices containing various mixtures of H_2O, CO_2, and CH_3OH at temperatures ranging from 5 to 150 K. The key difference between ices in groups (1) and (3) is the occurrence of crystallization features in the latter, which first appear at ~60 K. Each fit is calculated by combining spectra from two of these groups:

$$\tau(\lambda) = a_1 \tau_{\rm lab1}(\lambda) + a_2 \tau_{\rm lab2}(\lambda), \quad (1)$$

where $\tau_{\rm lab1}(\lambda)$ and $\tau_{\rm lab2}(\lambda)$ are the normalized optical depth spectra of the two laboratory ice components in the fit, and the scale factors a_1 and a_2 are free parameters. Component 1 is assumed to be a polar ice from group (1) in every case; component 2 is selected from the other groups, the final choice being determined by χ^2_ν minimization.

3.3. Results

Our laboratory fits, shown in Figures 2 and 3 and summarized in Table 2, are separated into two main evolutionary groups: (1) polar + nonpolar ("P+NP") and (2) polar + crystallized ice mixture ("P+CIM"). Recall that all fits within these two evolutionary groups were accomplished with the constraint of using only two ice components for each fit. See Table 2 for detailed fit information.

Spectra of YSOs in the P+NP group (Figure 2) exhibit CO_2 profiles that are best fit by a mix of polar CO_2 ice (i.e., CO_2 embedded in an H_2O matrix) and nonpolar CO_2 ice (i.e., CO_2 embedded in a CO matrix), all at temperatures $\lesssim$ 42 K. Some of the nonpolar laboratory ice spectra include O_2, but CO_2 or CO is always the dominant constituent. The observed profiles and resulting fits for objects in this group closely resemble those of background field stars such as Elias 16, CK2 and Q21-1 (Bergin et al. 2005; Whittet et al. 2009). We deduce that the lines of sight to the P+NP YSOs are sampling regions where the ices are thermally unevolved. This could arise because (1) absorption in the line of sight is dominated by cold foreground material in the molecular cloud and (2) material local to the YSO in the line of sight has not (yet) been heated significantly, or a combination of (1) and (2).

Spectra of YSOs in the P+CIM evolutionary group exhibit double-peaked structure in the 15 μm profile characteristic of crystallized CO_2 ices (Figure 3). Best fits combine polar and crystallized ice mixtures at temperatures 5–40 K and $\gtrsim$ 100 K, respectively. The profiles typically also display a shoulder at the long wavelength side of the feature attributed to complexing of CH_3OH with CO_2. As CH_3OH makes only a minor contribution to the total absorption in the feature, and the CIM ice component may not contain all the CH_3OH in a given line of sight, our fits are not expected to provide precise estimates of CH_3OH abundance toward individual sources. A range of 1%–15% with respect to H_2O is implied by our results (Table 2), consistent with that determined from observations at other wavelengths (e.g., Boogert et al. 2008). Evidence of crystallization suggests that ices toward these sources have been significantly heated, most probably as the result of exposure to infrared radiation from the embedded YSO, consistent with the assumption (Section 1) that an energy source is needed to drive efficient CH_3OH production.

4. EXTINCTION

In this section, we use near-infrared (*JHK*) photometry to estimate interstellar reddening and extinction toward sources in our sample. All available photometry is listed in Table 3 and is taken from the Two Micron All Sky Survey (2MASS;

[8] For example, Pontoppidan et al. (2008) report excellent fits to some 40 spectra in the c2d sample utilizing a superposition of five individual ice components derived from laboratory data and allowed to vary in amplitude from source to source; our fitting strategy differs from theirs in that we allow a suite of possible laboratory spectra for each of two components.

[9] We rejected any "polar" ice mixture containing more than 33% CO_2 relative to H_2O on the basis of existing observational constraints (e.g., Whittet et al. 2007, 2009; Knez et al. 2005; Zasowski et al. 2009).

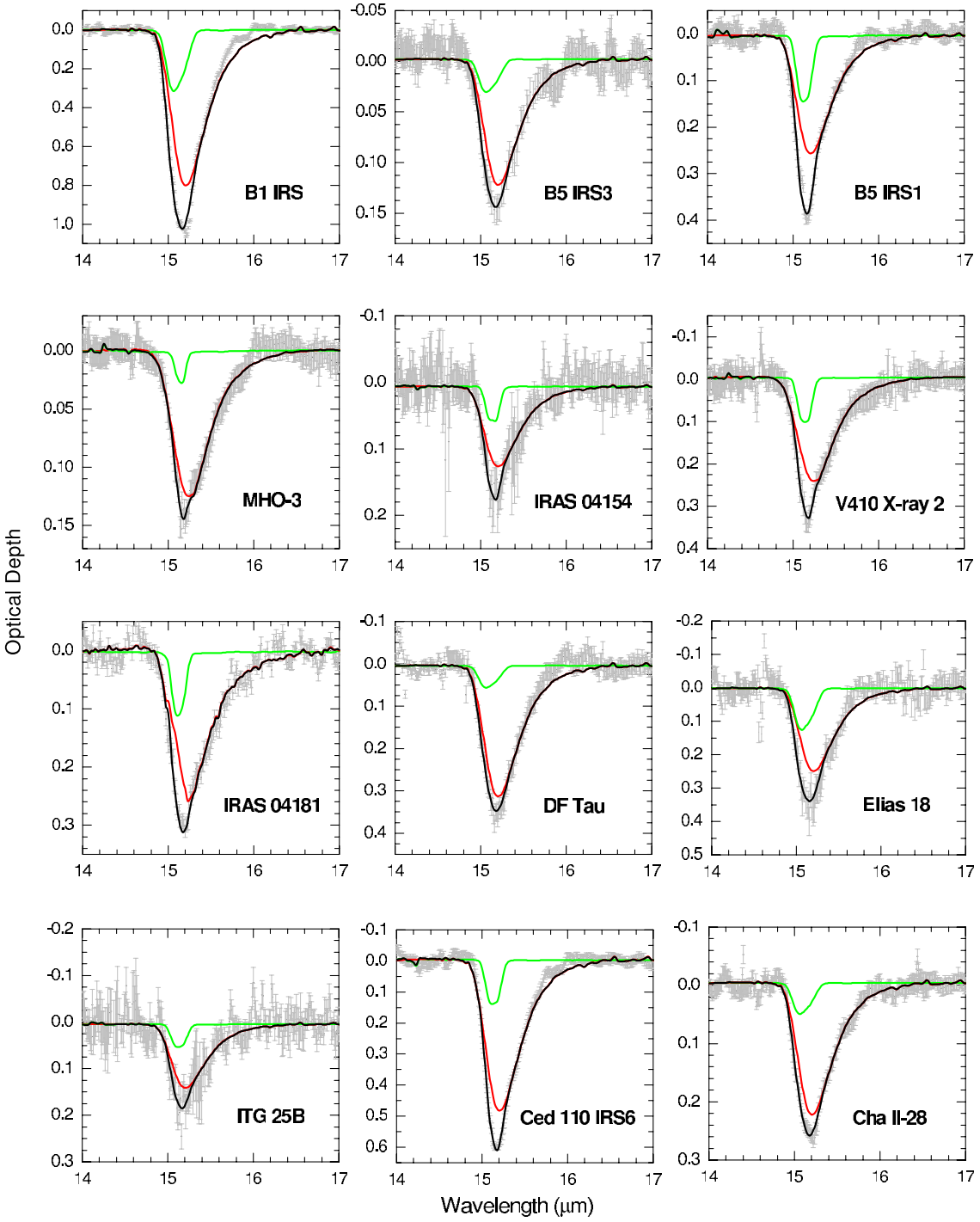

Figure 2. Results of χ^2_ν fitting routine, where the best mixture contained cold polar and nonpolar ices. Green lines indicate the nonpolar component used for the fit, red lines indicate the polar component, and black lines are the sum of the two components.

(A color version of this figure is available in the online journal.)

Skrutskie et al. 2006) unless otherwise indicated in the notes. The $J-H$, $H-K$ color–color diagram is shown in Figure 4 for the subset of 15 sources that have reliable photometry available in all three bands; reddened background field stars in the Taurus region (Whittet et al. 2007) are also plotted for comparison. In order to interpret the distribution of data in Figure 4 in terms of reddening, and convert to total extinction, an extinction law must be assumed, i.e., a form for the wavelength dependence of extinction. This is expected to vary according to the physical properties of the dust in a given environment, but the dispersion tends to be small in the infrared (e.g., Martin & Whittet 1990). We assume that the mean extinction law for dust in the Taurus dark cloud (Whittet et al. 2001, 2007) is applicable to our sample. The pertinent relationships describing this law are the slope of the reddening vector in the $J-H$, $H-K$ diagram:

$$E_{J-H} = 1.75 E_{H-K}, \quad (2)$$

where E represents color excess (i.e., reddening), and the conversion from reddening in the infrared to total (visual) extinction:

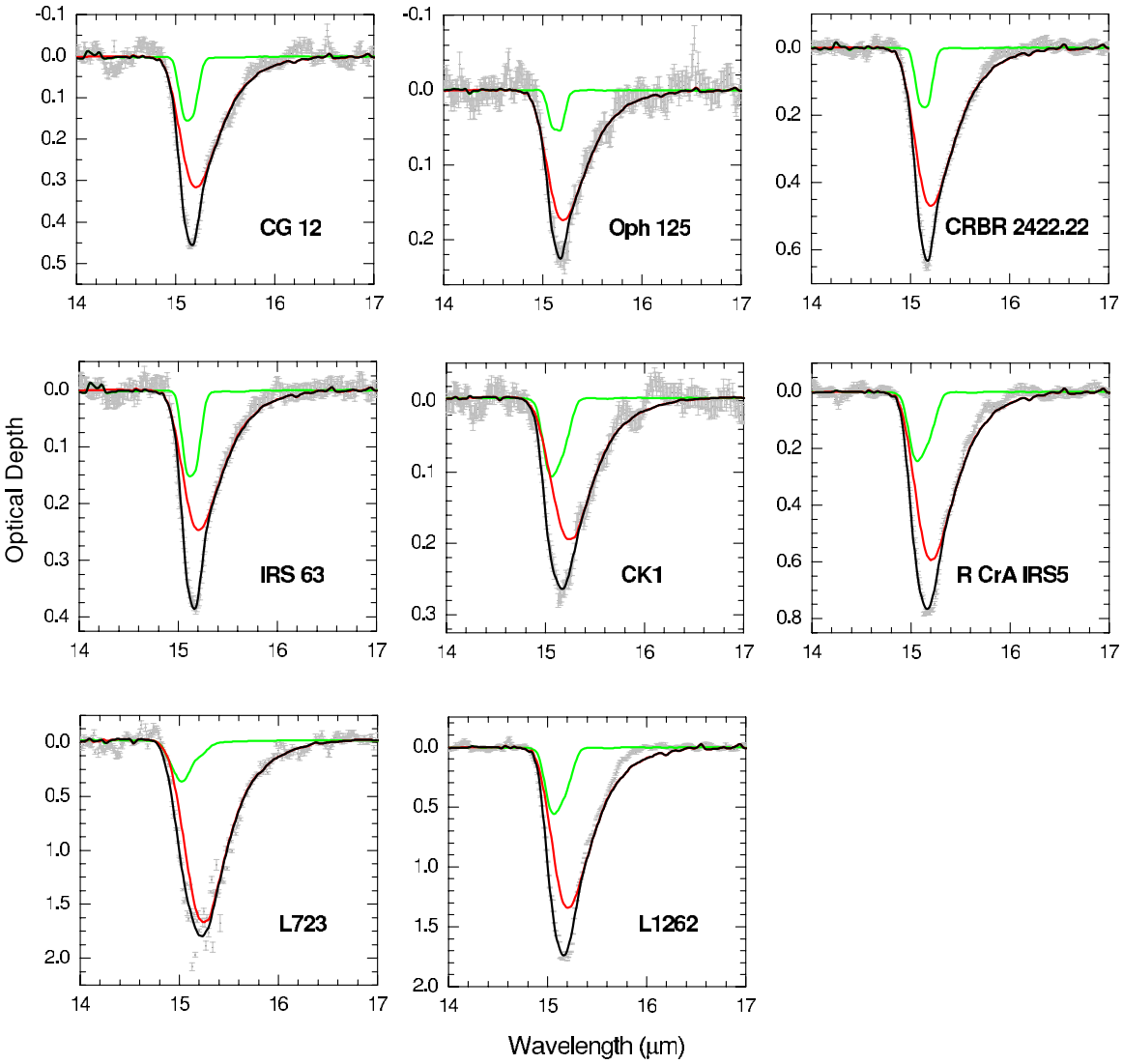

Figure 2. (Continued)

$$A_V = 5.2E_{J-K} = 5.2(E_{J-H} + E_{H-K}). \quad (3)$$

The solid diagonal lines in Figure 4 have a slope of 1.75 (Equation (2)) and denote the upper and lower bounds of the region where normal reddened stars are expected to reside. A few YSOs in our sample plot with the field stars in this region, but the majority lie below and to the right, in the zone between the lower solid line and the dashed line. This is expected in cases where infrared emission from heated circumstellar dust is present, introducing additional flux at the longer wavelengths. An excess in $H-K$ implies that dust close to the YSO reaches temperatures ∼1000 K, i.e., well above those responsible for sublimation and crystallization of ices; thus, a one-to-one correspondence between $H-K$ excess and evidence of thermal processing in the ice spectra is not expected. We note that 2 out of 2 P+CIM sources and 9 out of 13 P+NP sources show evidence of significant $H-K$ excess in Figure 4. In the latter case, the lack of evidence for annealing suggests that most of the ice toward these YSOs is in cold molecular cloud material remote from the source rather than the warm circumstellar disk or envelope: warm dust close to the source may contribute only a small fraction of the total opacity.

For YSOs occupying the field-stars region in Figure 4, estimation of the extinction is straightforward, following the method used by Shenoy et al. (2008): in each case the displacement required to deredden the star onto intrinsic color lines provide measures of E_{J-H} and E_{H-K} in Equation (3). The intrinsic colors of the YSOs are generally unknown or poorly constrained and the range of possible displacements results in errors of ±2 mag in the estimated values of A_V (Table 3). For YSOs in the circumstellar excess region, we assume that contamination affects only $H-K$ and not $J-H$ (reasonable for dust temperatures $\lesssim$1000 K) and estimate $A_V = 8.2E_{J-H}$ (Equations (2) and (3)), assuming a mean intrinsic color $(J-H)_0 = 0.6$.

5. COLUMN DENSITIES AND CORRELATIONS

Using our optical depth spectra, column densities were calculated from the relation

$$N(\mathrm{CO_2}) = \frac{1}{A}\int \tau d\nu, \quad (4)$$

where τ is the optical depth, ν (cm^{-1}) is the wavenumber, and A (cm molecule^{-1}) is the band strength of the CO_2 absorption

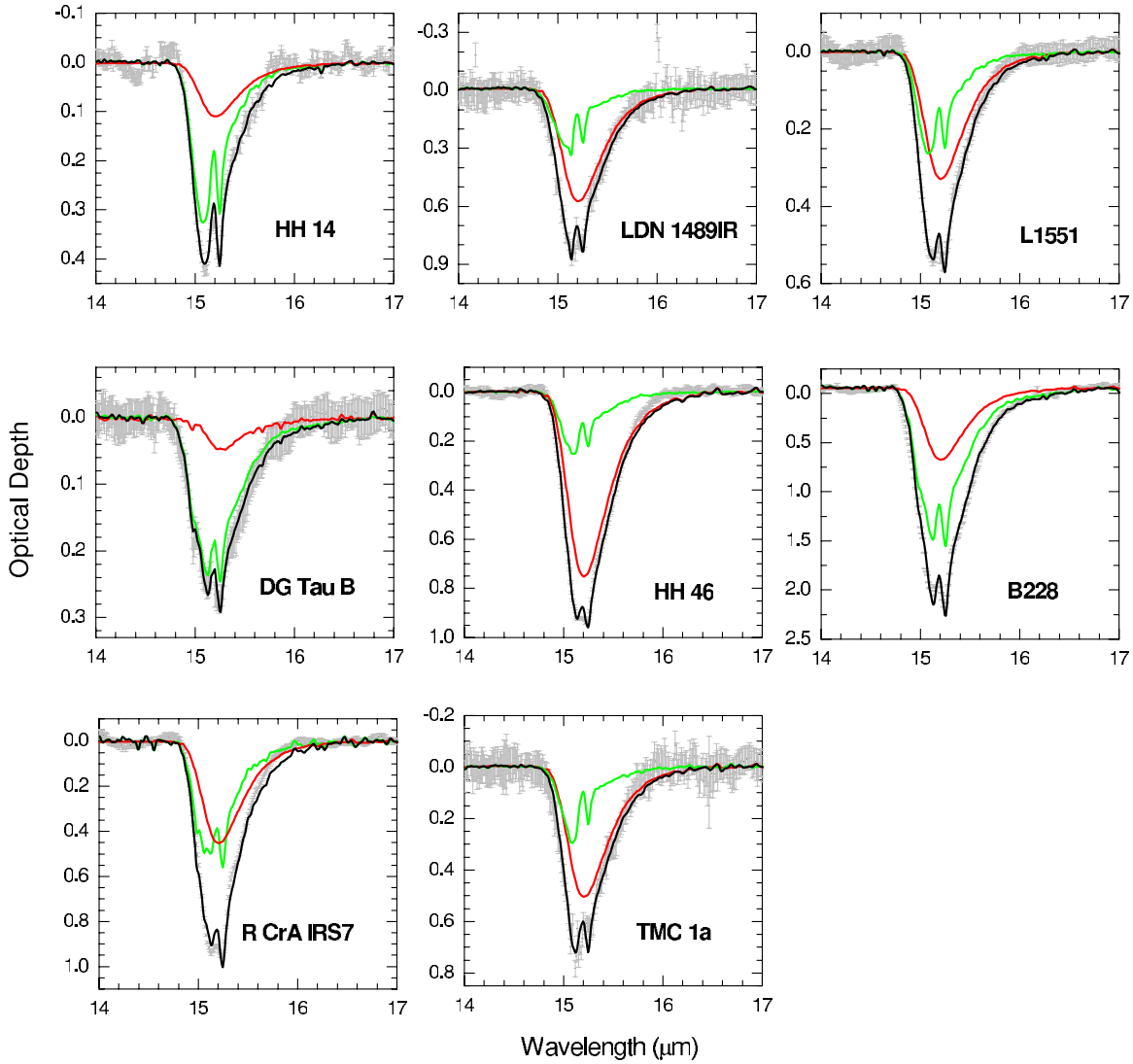

Figure 3. Results of the χ^2_ν fitting routine, where the best mixture contained cold polar ice and a crystallized ice mixture (CIM). Green lines indicate the CIM component, red lines indicate the polar component, and black lines are the sum of the two components.

(A color version of this figure is available in the online journal.)

feature. Band strengths are measured in the laboratory to accuracies of typically a few percent. Gerakines et al. (1995) showed that the band strength of pure solid CO_2 at 15 μm is not significantly different from that of CO_2 diluted in an H_2O matrix, i.e., the results agree to within the experimental uncertainties. We therefore adopt the pure CO_2 band strength (1.1×10^{-17} cm molecule^{-1}) for consistency with most previous work (Gerakines et al. 1999; Nummelin et al. 2001; Pontoppidan et al. 2008; Whittet et al. 2007, 2009). Note that column densities from Zasowski et al. (2009) should be scaled up by a factor of 1.36 (i.e., 1.5/1.1) for comparison with our results and those from the papers listed above, to allow for the different band strength assumed by these authors.

Each optical depth spectrum (Figures 2 and 3) was integrated between bounds chosen on a case-by-case basis. This was done to ensure that the entire solid CO_2 feature was always included, notwithstanding small source-to-source variations in the position and width of the feature. The typical wavelength range of the integration was 14.8–16.3 μm. Table 3 lists column density results for both total CO_2 and the polar, nonpolar, and crystallized CO_2 components arising from the profile fitting (Section 3), along with literature values for H_2O and CO. Uncertainties in our results take into account both continuum fitting uncertainties (Section 2.3) and noise in the observational data.

5.1. Correlation with Extinction

Extinction (A_V) effectively measures the mean dust column density in a given line of sight. Figure 5 plots total $N(CO_2)$ versus A_V, as available, for YSOs in our sample (Table 3). Also shown for comparison are data for background field stars toward three clouds. Field stars located behind the best sampled cloud (Taurus) yield a strong linear correlation (correlation coefficient $R = 0.97$), the intercept of which indicates an extinction threshold, i.e., the minimum extinction for solid CO_2 detection, of 4.3 ± 1.0 mag (Whittet et al. 2007). Data for field stars behind other clouds are currently limited to just two lines of sight, CK2 in Serpens and Q21-1 in IC5146 (Whittet et al. 2009). It is notable that the distribution of YSOs in Figure 5 also suggests a linear trend, if three outliers are disregarded, but with a CO_2 abundance per unit extinction that is systematically

Table 2
Summary of Laboratory Fits

Fit Group	Source Name	Polar Ice	T (K)	τ	Nonpolar/CIM Ice	T (K)	τ	χ^2_ν
Polar + Nonpolar	B1 IRS	H_2O:CO_2:CO=100:20:3	20	0.802	CO:CO_2=100:70	10	0.316	28.6
	B5 IRS3	H_2O:CO_2:CO=100:20:3	20	0.124	CO:CO_2=100:23	10	0.032	0.24
	B5 IRS1	H_2O:CO_2:CO=100:20:3	20	0.254	CO:CO_2=100:26	10	0.142	2.64
	MHO-3	H_2O:CO_2=100:14	10	0.125	CO:O_2:CO_2=10:20:11	10	0.028	0.39
	IRAS 04154+2823	H_2O:CO_2:CO=100:20:3	20	0.120	CO:O_2:CO_2=100:50:16	10	0.052	0.54
	V410 X-ray 2	H_2O:CO_2=100:14	10	0.244	CO:O_2:CO_2=100:11:20	10	0.105	0.19
	IRAS 04181+2654	H_2O:CO_2=5:1	30	0.257	CO:CO_2=100:23	30	0.110	2.39
	DF Tau	H_2O:CO_2:CO=100:20:3	20	0.301	CO:CO_2=100:70	10	0.052	1.18
	Elias 18	H_2O:CO_2:CO=100:20:3	20	0.504	H_2O:CH_3OH:CO_2=1:1.5:1	110	0.303	1.03
	ITG 25B	H_2O:CO_2:CO=100:20:3	20	0.137	CO:CO_2=100:26	10	0.049	0.97
	Ced 110 IRS6	H_2O:CO_2:CO=100:20:3	20	0.485	CO:O_2:CO_2=100:10:23	10	0.142	3.03
	Cha II-28	H_2O:CO_2:CO=100:20:3	20	0.226	CO:CO_2=100:70	10	0.053	0.64
	CG 12	H_2O:CO_2:CO=100:20:3	20	0.315	CO:CO_2=100:26	10	0.155	2.24
	Oph 125	H_2O:CO_2:CO=100:20:3	20	0.174	CO:O_2:CO_2=100:50:16	10	0.054	0.94
	CRBR 2422.8-3423	H_2O:CO_2:CO=100:20:3	20	0.468	CO:O_2:CO_2=100:11:20	10	0.176	2.85
	IRS 63	H_2O:CO_2:CO=100:20:3	20	0.246	CO:CO_2=100:26	10	0.152	1.61
	CK 1	H_2O:CO_2=100:14	10	0.198	CO:CO_2=100:70	10	0.110	0.79
	R CrA IRS5	H_2O:CO_2:CO=100:20:3	20	0.592	CO:CO_2=100:70	10	0.243	8.56
	L723	H_2O:CO_2=100:14	10	1.684	H_2O:CO_2=1:6	42	0.379	34.4
	L1262	H_2O:CO_2:CO=100:20:3	20	1.340	CO:CO_2=100:70	10	0.557	150.0
Polar + CIM	HH 14	H_2O:CO_2:CO=100:20:3	20	0.107	H_2O:CH_3OH:H_2O=2:0.5:1	135	0.324	2.91
	L1489 IR	H_2O:CO_2:CO=100:20:3	20	0.583	H_2O:CH_3OH:CO_2=1:1:1	115	0.344	0.90
	DG Tau B	H_2O:CO_2=10:1	40	0.047	H_2O:CH_3OH:CO_2=2:0.5:1	125	0.245	0.25
	L1551 IRS5	H_2O:CO_2:CO=100:20:3	20	0.328	H_2O:CH_3OH:CO_2=2:0.5:1	110	0.262	0.89
	TMC-1A	H_2O:CO_2:CO=100:20:3	20	0.506	H_2O:CH_3OH:CO_2=2:1.5:1	110	0.297	1.04
	HH 47 IR	H_2O:CO_2:CO=100:20:3	20	0.751	H_2O:CH_3OH:CO_2=2:1:1	125	0.253	8.00
	B228	H_2O:CO_2:CO=100:20:3	20	0.728	H_2O:CH_3OH:CO_2=2:0.5:1	125	1.611	110.0
	R CrA IRS7a	H_2O:CO_2:CO=100:20:3	20	0.451	H_2O:CH_3OH:CO_2=2:0.1:1	140	0.559	19.1

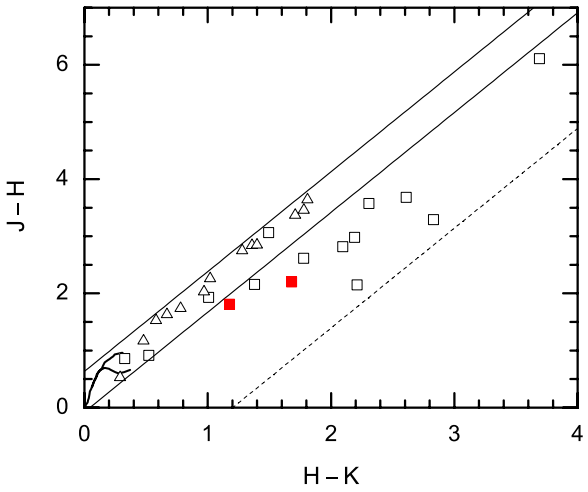

Figure 4. *JHK* color–color diagram for YSOs from this paper and Taurus field stars from Whittet et al. (2007). Triangles denote field stars, open squares denote P+NP YSOs, and filled (red) squares denote P+CIM YSOs. Photometry for Ced 110 IRS6 is from Persi et al. (2001); all other photometry is from the 2MASS database (Table 3). Solid curves near the origin are intrinsic colors, indicating the expected loci of normal unreddened stars of luminosity classes III and V. Normal reddened stars are expected to lie between the solid diagonal lines for an extinction law $E_{J-H} = 1.75E_{H-K}$ (Whittet et al. 2007). YSOs with significant infrared excess emission at 2 μm are expected to reside in the zone between the lower solid line and the dashed line.

(A color version of this figure is available in the online journal.)

~30% higher. All YSOs that follow this general trend have P+NP classification from our fitting procedure, i.e., their CO_2 profiles resemble those of field stars. It should also be noted that two "non-Taurus" field stars (CK2 and Q21-1) plot with the YSOs, having significantly more CO_2 per unit extinction than expected based on the Taurus correlation. One interpretation is that the Taurus cloud is not prototypical (see Whittet et al. 2009 for further discussion) and that CO_2 abundance per unit dust column exhibited by CK2 and Q21-1 is more representative of ice chemistry: in this case, the CO_2 abundance found in the P+NP YSOs may be attributed entirely ices in the foreground with no local enhancement. However, considering data for the Taurus cloud alone (solid black symbols), we see a significant difference in the trends for field stars and YSOs. This suggests the possibility of local CO_2 production toward the YSOs.

We next consider the outliers displaying large apparent CO_2 enhancements relative to A_V in Figure 5. Two out of the three in this group (L1551 IRS5 and HH14) are P+CIM sources, and it seems plausible that CO_2 production is driven by a local radiation field in these lines of sight that is also responsible for crystallization of the ices. However, an alternative (and less interesting) explanation could arise if the observed values of A_V and $N(CO_2)$, which are estimated from near- and mid-infrared data, respectively, do not sample the exact same column of dust. This latter explanation seems particularly likely in the case of DF Tau, which is expected to have negligible CO_2 abundance on the basis of its very low apparent A_V. DF Tau is a binary system in which one component is undergoing flare activity (Li et al. 2001; Lamzin et al. 2001). If the dust distribution is uneven, it may be the case that the star with the lowest extinction dominates the near-infrared flux and the star with the highest extinction dominates the flux at 15 μm.

5.2. Correlation with Other Ices

We next consider the intercorrelation of ice column densities in our sample. Figures 6 and 7 plot available $N(H_2O)$ versus

Table 3
Magnitudes, Extinctions, and Column Densities[a]

Source	J	H	K	A_V	α	$N(CO_2)$	$N(H_2O)$	$N(CO)$	$N(CO_2)$ Polar	$N(CO_2)$ Nonpolar	$N(CO_2)$ Crystallized	Notes[b]
HH 14	15.00	13.19	12.01	11.0	1.09	9.48 ± 0.55	40.5 ± 3.7	3.1 ± 1.6	3.01	...	6.46	1
B1 IRS	...	...	14.21	...	1.81	24.1 ± 0.2	104 ± 23	...	20.11	4.01	...	1
B5 IRS3	16.41	14.26	12.05	13.0	0.75	3.23 ± 0.25	10.1 ± 0.9	2.9 ± 1.3	2.82	0.41	...	1
B5 IRS1	17.34	14.05	11.21	23.0	1.22	8.34 ± 0.20	22.6 ± 2.8	11.5 ± 1.9	6.89	1.44	...	1
L1489 IR	...	...	...	...	...	19.3 ± 1.7	47 ± 2.8	9.0 ± 0.5	13.29	...	5.98	1
MHO-3	11.18	9.25	8.24	11.0	...	3.57 ± 0.33	...	...	3.32	0.25	...	
IRAS 04154+2823	15.19	12.37	10.27	19.0	0.21	4.47 ± 1.27	8.75 ± 0.8	...	4.02	0.45	...	2
V410 X-ray 2	13.77	10.71	9.22	19.6	−0.18	6.85 ± 0.24	...	...	5.86	0.98	...	
IRAS 04181+2654	16.22	12.65	10.34	25.0	0.30	7.67 ± 0.24	25 ± 2	7.7 ± 0.8	6.31	1.35	...	2
DG Tau B	15.60	...	...	...	...	7.49 ± 0.74	26.3 ± 2.6	2.8 ± 1.4	1.42	...	6.06	1
DF Tau	8.17	7.26	6.73	3.0	−1.04	9.22 ± 0.65	...	...	8.54	0.68	...	
L1551 IRS5	13.71	11.51	9.82	14.0	1.93	13.70 ± 0.61	...	...	8.39	...	5.31	
TMC-1A	...	13.752	10.84	...	1.29	17.52 ± 0.62	...	...	12.41	...	5.10	
Elias 18	10.67	8.05	6.28	22.2	−0.51	6.65 ± 0.47	14 ± 1.4	3.1 ± 0.3	5.35	1.3	...	3
ITG 25B	12.41	10.25	8.87	12.5	−0.50	4.63 ± 0.57	16 ± 1.6	2.0 ± 0.2	4.12	0.50	...	2
HH 47 IR	...	...	...	...	...	23.91 ± 0.24	77.9 ± 7.3	15.6 ± 1.6	18.88	...	5.02	1
Ced 110 IRS6	20.99	14.74	10.92	46.0	0.66	12.97 ± 0.31	47 ± 6	26.3 ± 4.0	11.63	1.34	...	1, 6
Cha II-28	...	13.90	10.66	...	0.89	5.71 ± 0.25	29.8 ± 5.6	...	5.03	0.67	...	1
CG 12	14.84	...	10.42	...	0.31	9.74 ± 0.54	20.7 ± 2.0	...	8.16	1.58	...	1
B228	...	...	14.32	...	1.82	50.5 ± 0.5	148 ± 40	...	9.71	...	40.80	1
Oph 125	...	14.69	10.56	51.6	...	4.91 ± 0.51	36.5 ± 5	3.9 ± 0.6	4.44	0.46	...	1
CRBR 2422.8-3423	...	...	13.68	...	...	13.50 ± 0.20	45 ± 5	31.1 ± 4.0	11.85	1.64	...	1
IRS 63	15.50	11.83	9.22	26.0	0.34	7.82 ± 0.40	20.4 ± 3	14.2 ± 0.4	6.27	1.55	...	1
CK 1	12.22	9.24	7.05	20.0	...	6.12 ± 0.44	16.9 ± 1.6	6.5 ± 0.7	4.72	1.39	...	1, 4
R CrA IRS5	...	13.65	...	...	...	18.26 ± 0.22	37.6 ± 2.8	6.3 ± 0.4	15.17	3.08	...	1, 5
R CrA IRS7a	12.55	...	...	...	...	23.50 ± 0.23	109 ± 19	10.0 ± 1.0	11.59	...	11.91	1, 3
L723	...	...	...	...	0.50	49.0 ± 4	...	...	44.22	4.75	...	7
L1262	...	15.70	13.92	...	1.47	41.5 ± 0.5	130 ± 23	...	34.40	7.05	...	1

Notes.
[a] All column densities are in units of 10^{-17}cm^{-2}.
[b] H_2O and CO column densities are from (1) Pontoppidan et al. (2003, 2008); (2) unpublished IRTF data (J. E. Chiar et al. 2011, in preparation); (3) Chiar et al. (1998); (4) Chiar et al. (1994); (5) Tanaka et al. (1994). Additional notes: (6) Photometry for Ced 110 IRS6 is from Persi et al. (2001) (this source lacks reliable J photometry from *2MASS*). (7) The 2MASS point source closest to the position of L723 (J19175313+1912163) appears to be an unrelated field star.

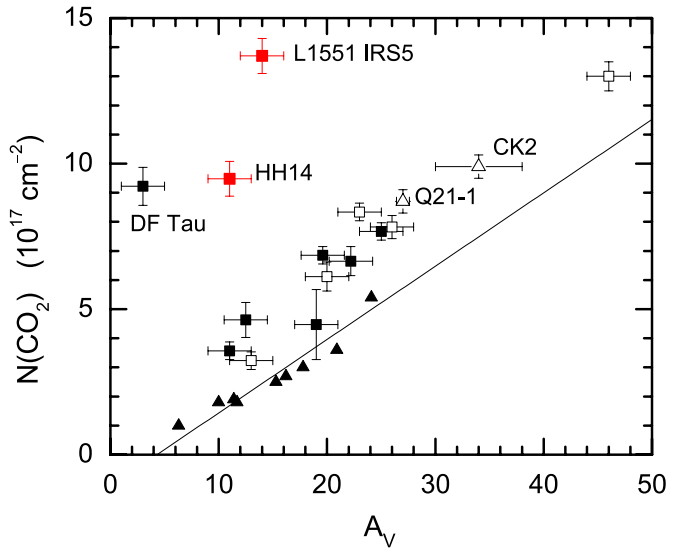

Figure 5. Plot of CO_2 ice column density against visual extinction for YSOs from the present work (squares) and background field stars from Whittet et al. (2007, 2009; triangles). YSOs with P+CIM classification are filled in red; all other YSOs have P+NP classification. Stars located in the direction of the Taurus dark cloud are distinguished by black filled symbols. The solid line is the linear least-squares fit to Taurus field stars only.
(A color version of this figure is available in the online journal.)

$N(CO_2)$ data for YSOs, including our results (Table 3) and those from previous literature (Pontoppidan et al. 2008; Nummelin et al. 2001; Gerakines et al. 1999), together with field stars from Whittet et al. (2007, 2009). Figure 6 shows the overall correlation, Figure 7 is rescaled to show greater detail near the origin and with separate panels for all objects (above) and only Taurus objects (below). Taurus field stars show a particularly tight linear correlation ($R = 0.99$) passing through the origin to within statistical error:

$$N(CO_2)[\text{field}] = (0.18 \pm 0.04)N(H_2O) \quad (5)$$

(Whittet et al. 2007; solid lines in Figures 6 and 7), indicating that these two species form in tandem in this quiescent cloud. The distribution of YSOs is also consistent with a linear correlation through the origin (a free fit yielding a negligible intercept); in this case, the correlation coefficient is $R = 0.97$, and the slope is steeper in comparison to the correlation for Taurus field stars:

$$N(CO_2)[\text{YSO}] = (0.29 \pm 0.01)N(H_2O) \quad (6)$$

(dotted line in Figure 6 and the upper panel of Figure 7). Gerakines et al. (1999) found no significant dependence of the $N(CO_2)/N(H_2O)$ ratio on environment in a smaller sample of predominantly high-mass YSOs and field stars, both falling

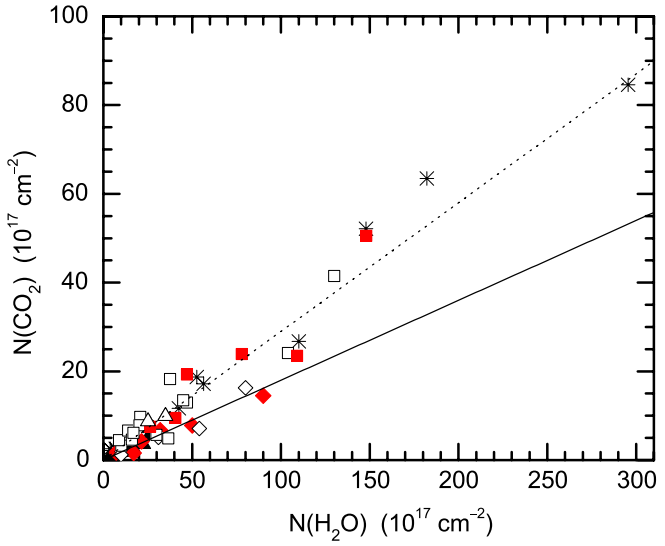

Figure 6. Plot of $N(CO_2)$ vs. $N(H_2O)$ (see also Figure 7 for an enlargement of the region near the origin). Filled and open triangles denote field stars behind Taurus and other clouds, respectively (Whittet et al. 2007, 2009). All other symbols denote YSOs: P+NP YSOs from this paper (open squares); P+CIM YSOs from this paper (red squares); P+NP YSOs from Gerakines et al. (1999, open diamonds); P+CIM YSOs from Gerakines et al. (1999, red diamonds); YSOs from Pontoppidan et al. (2008, asterisks); YSOs from Nummelin et al. (2001, crosses). The dotted and solid lines are linear least-squares fits to the correlations for all YSOs and Taurus field stars, respectively.

(A color version of this figure is available in the online journal.)

within essentially the same trend: $N(CO_2)/N(H_2O) = 0.17 \pm 0.03$. However, extended samples that include lower mass YSOs indicate that this ratio does display a degree of dependence on environment, our present work confirming the findings of Pontoppidan et al. (2008). The steeper slope of the YSO correlation line in comparison to the field-star correlation line in Figure 6 suggests enhanced production of CO_2 in the environments of some YSOs. However, as a caveat, we note that CO_2 abundances more in line with the YSO values are found for two non-Taurus field stars (CK2 in Serpens; in Q21-1 in IC5146; Knez et al. 2005; Whittet et al. 2009). The Taurus region is sufficiently well observed to allow a comparison of YSOs and field stars in the same cloud, and this is shown in Figure 7 (lower panel). This plot illustrates that, on average, Taurus YSOs have CO_2 abundances a factor of ~2 higher relative to H_2O compared with Taurus field stars.

Figure 8 shows the corresponding correlation between $N(H_2O)$ and $N(CO)$, again using all available data from the current work and previous literature cited above. The correlation lines for field stars and YSOs are

$$N(\mathrm{CO})[\mathrm{field}] = (0.47 \pm 0.1)N(\mathrm{H_2O}) - (3.16 \pm 2.0) \quad (7)$$

$$N(\mathrm{CO})[\mathrm{YSO}] = (0.12 \pm 0.1)N(\mathrm{H_2O}) + (2.31 \pm 2.0). \quad (8)$$

In this case, the YSOs show a much greater degree of scatter compared with field stars (the correlation coefficients are $R = 0.45$ and 0.89, respectively). As CO is more volatile than H_2O or CO_2, it is expected to sublimate far more readily upon heating. The data in Figure 8 are consistent with varying degrees of CO sublimation, determined by the local environment in the vicinity of each YSO. This conclusion is supported by the fact that YSOs in the P+CIM group tend to have systematically lower CO column densities compared with the average for all YSOs.

Column density estimates for the components of our profile fits may be used to investigate their intercorrelation. Our fitting

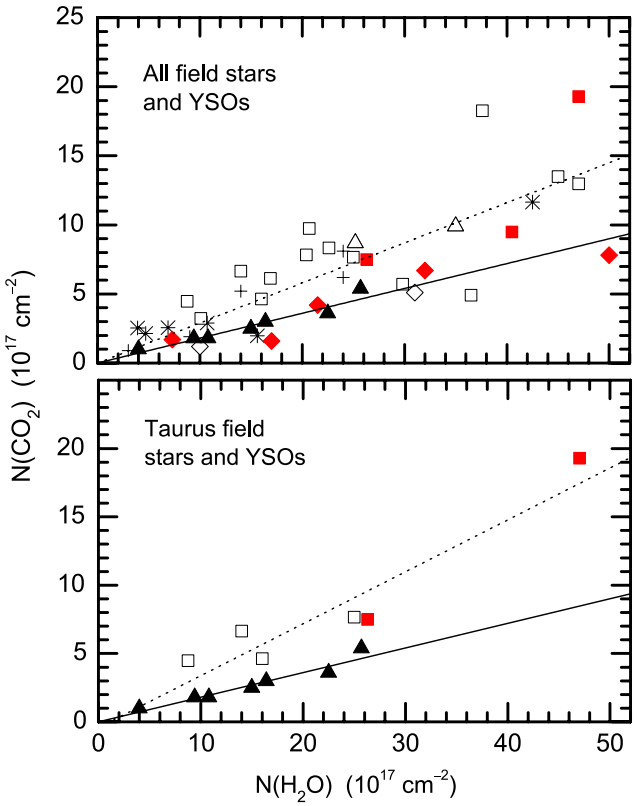

Figure 7. Plots of $N(CO_2)$ vs. $N(H_2O)$, similar to Figure 6, but rescaled to show greater detail near the origin and with separate panels for all objects (above) and only Taurus objects (below). Symbols have the same meaning as in Figure 6. The dotted lines are fits to all YSOs and Taurus YSOs in the upper and lower panels, respectively; the solid line in each panel is the fit to Taurus field stars.

(A color version of this figure is available in the online journal.)

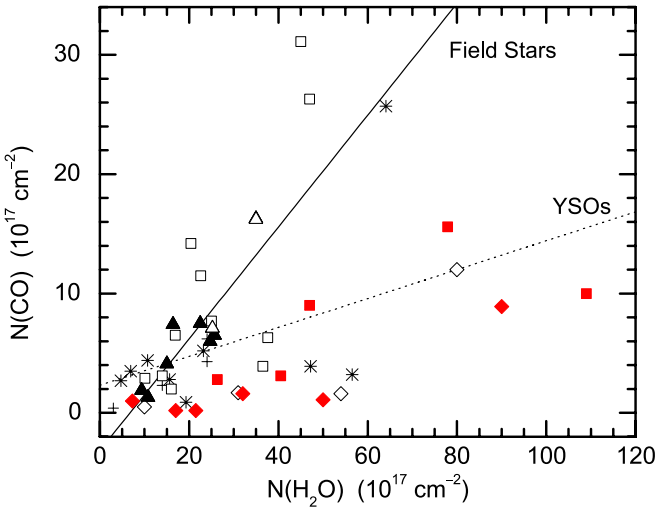

Figure 8. Plot of $N(CO)$ vs. $N(H_2O)$. Symbols have the same meaning as in Figure 6. The dotted and solid lines are the least-squares fits to the correlations for YSOs and field stars, respectively.

(A color version of this figure is available in the online journal.)

procedure (Section 3.2) assumes that two of three possible mixtures (cold polar, cold nonpolar, and warmed ices) are contributing to the observed 15 μm feature, and that all lines of sight include a polar component. The four panels of Figure 9 plot $N(CO_2)$ values for each relevant component and for the total (Table 3), in each case against $N(H_2O)$. The parameters of the

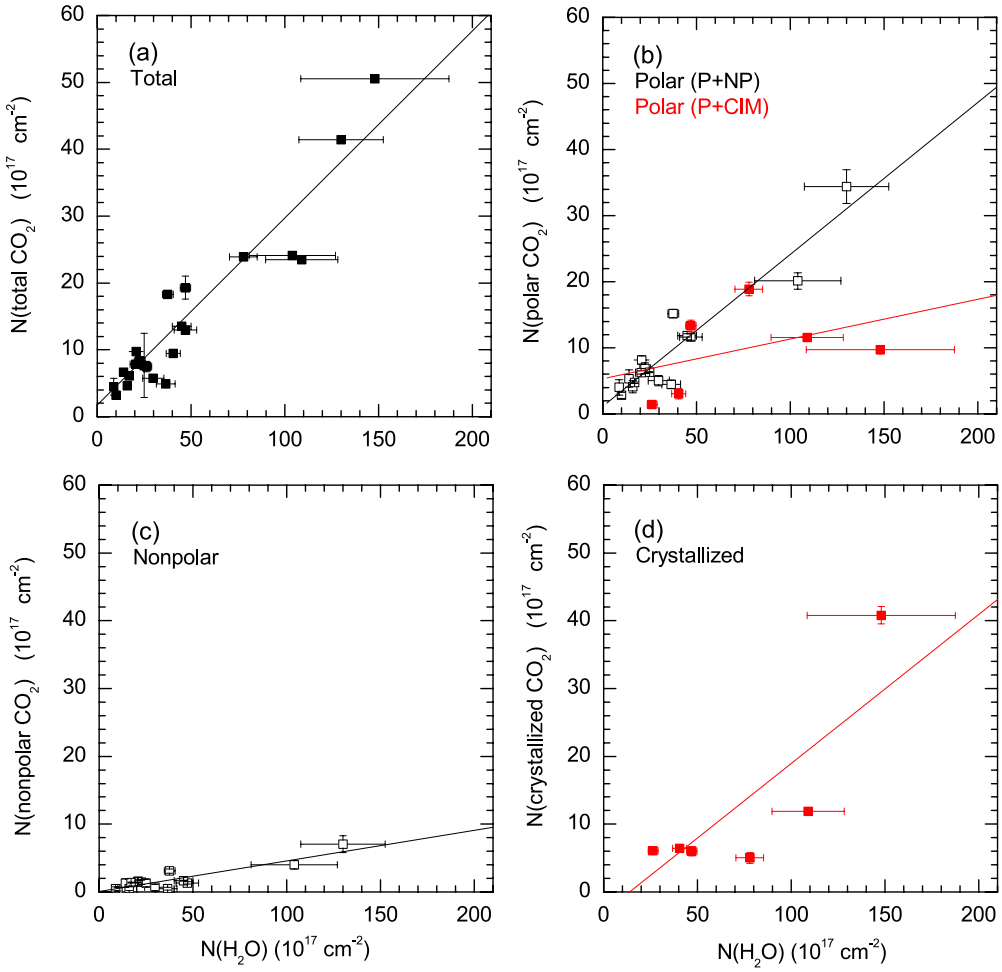

Figure 9. Correlations of $N(CO_2)$ ice components with $N(H_2O)$, based on our laboratory fits to the 15 μm CO_2 feature for YSOs in our sample (Tables 2 and 3). The panels represent (a) total, (b) polar, (c) nonpolar, and (d) crystallized CO_2. Red squares and black open squares represent P+CIM sources and P+NP sources, respectively; black squares represent the total (polar, nonpolar, crystallized) CO_2 for all sources. Lines represent the linear least-squares fit for each correlation; in panel (b), the black and red lines are fits to P+NP and P+CIM data, respectively.

(A color version of this figure is available in the online journal.)

Table 4
Correlation Lines for Figure 9

Correlation Line[a] $N(H_2O)$ versus	Slope	Intercept	Correlation Coefficient	Panel in Figure 9
Total CO_2	0.28 ± 0.03	1.72 ± 1.6	0.95	a
Polar CO_2, P+NP only	0.23 ± 0.02	1.16 ± 1.0	0.94	b, black line
Polar CO_2, P+CIM only	0.06 ± 0.06	5.35 ± 5.5	0.41	b, red line
Nonpolar CO_2	0.04 ± 0.01	0.09 ± 0.3	0.90	c
Crystallized CO_2	0.22 ± 0.07	−3.06 ± 5.5	0.84	d

Note. [a] Format: $N(CO_2) = c_1 N(H_2O) + c_2$, where c_1 and c_2 are the slope and intercept.

fits are listed in Table 4. Figure 9 (panel (a)) confirms the strong correlation between $N(H_2O)$ and total $N(CO_2)$ for our sample, as expected on the basis of Figure 6. A high degree of correlation is also seen in both the polar and nonpolar components of the P+NP sources individually (panels (b) and (c) of Figure 9). This is in contrast to the situation for the P+CIM group, which display greater scatter and a trend in CO_2 abundance toward lower concentrations in the polar ice component and relatively high concentrations in the crystallized component (panels (b) and (d)).

The origin of the crystallized ice component is an important question (see Pontoppidan et al. 2008 for detailed discussion). The apparent reduction in polar ices toward some YSOs with crystalline components (Figure 9) is consistent with a scenario in which it is predominantly the polar ices that are being crystallized; the total abundance of CO_2 in the mantles is conserved during the crystallization process, with scatter arising from different levels of thermal processing in each line of sight. The polar ices are, indeed, the primary reservoir of CO_2 in the ices and high abundances of crystalline CO_2 can only arise if that reservoir is tapped. However, the laboratory CIM analogs used in our fits are presumed to be only partially crystallized, and the total abundance of crystallized CO_2 needed to explain the subfeatures in the profiles may thus be relatively small.

Pontoppidan et al. (2008) propose that crystallization of CO_2 accompanies distillation of the nonpolar ices as CO sublimates, which may be more probable in the envelopes of low-luminosity YSOs as it can occur at substantially lower temperatures (20–40 K) than those required for thermal processing of the polar ices (>50 K). Our results do not provide a definitive answer to this question but they do suggest that the polar ices may contribute to crystalline CO_2.

5.3. The Ternary Plot

As previously noted, observations show H_2O, CO, and CO_2 to be the most abundant constituents of ices in molecular clouds. A ternary plot is a useful analytical tool for studying a system with three primary constituents, allowing a two-dimensional representation of the relative contributions of each to the total.[10] Figure 10 presents ternary plots for the H_2O-CO-CO_2 system in interstellar ices (plots displaying all available data and data for the Taurus region only are shown). A pure ice composed entirely of one of these molecules would plot at the relevant vertex of the triangle (left, right, or top vertex for CO, H_2O, or CO_2, respectively). The scales on the sides of the triangle denote relative abundances, and the values for a given point should be read along lines parallel to the tick marks for each axis. As H_2O is by far the most abundant of the three, it is scaled by a factor of 0.2 so that an "average" ice composition falls near the center of the plot (rather than near the H_2O vertex). Each plotted point represents a line of sight in which reliable data exist for all three constituents, its position determined by the fractional abundance of each relative to the sum. YSOs from the present paper and from Pontoppidan et al. (2008) are included, together with field stars from our previous work (Whittet et al. 2007, 2009). Field stars and YSOs (P+NP or P+CIM classification) are distinguished by plotting symbol. Examples of possible evolutionary trends are illustrated by the insets: variation in CO concentration independent of H_2O:CO_2 ratio, as might arise from thermal processing of nonpolar ices (I); and variation in H_2O:CO_2 ratio independent of CO concentration, as might arise from differences in the surface chemistry that forms the polar ices (II).

Background field stars (triangles) in Figure 10 follow a distribution broadly consistent with variations in CO abundance independent of the relative proportions of the other two constituents. As most of the CO in a typical line of sight resides in the volatile nonpolar component of the mantles, this distribution can be interpreted as a trend of condensation versus sublimation of nonpolar ices (diagonal trend toward and away from the CO vertex of the plot, respectively, as indicated by the dotted lines and inset I in Figure 10). The loci of individual field stars along the trend correlate loosely with A_V, reflecting a greater preponderance of CO in the mantles for lines of sight containing denser (more optically thick) regions within the molecular clouds. Scatter orthogonal to the trend indicates variations in CO_2:H_2O ratio. Comparison of the field-star and YSO distributions reveals both similarities and differences. The distribution of P+NP YSOs (black squares) generally resembles

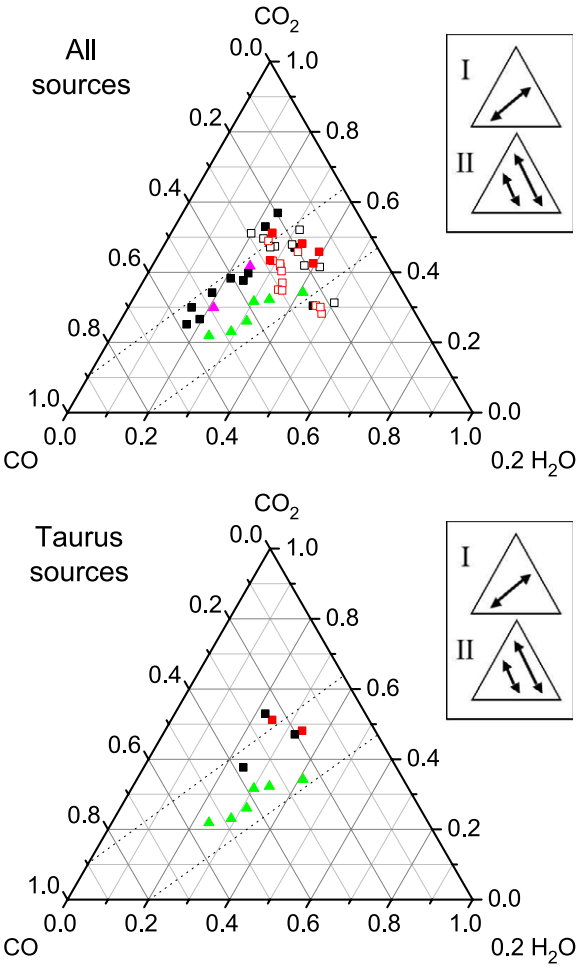

Figure 10. Ternary diagrams for H_2O, CO, and CO_2 in interstellar ices. All available data are plotted in the upper panel; the lower panel is limited to lines of sight in the Taurus region. The H_2O axis is scaled by a factor of 0.2 so that ices with average composition plot near the center of each plot. Triangles denote field stars behind Taurus (green) and other clouds (magenta) (Whittet et al. 2007, 2009). Squares denote YSOs from the current work (filled) and Pontoppidan et al. (2008, open), colored red in cases where the CO_2 profile indicates a crystallized ice component. Examples of possible evolutionary trends are illustrated by the insets. See Section 5.3 for further explanation and discussion.

(A color version of this figure is available in the online journal.)

that of field stars, i.e., consistent with a trend dominated by CO condensation/sublimation, but with a tendency for greater scatter as the CO abundance becomes smaller. P+CIM YSOs (red squares) are segregated away from the CO vortex, as expected given that they show independent evidence for thermal processing: the heating responsible for crystallization seems likely to result in simultaneous (partial) sublimation of the volatile nonpolar CO-rich ice component.

The vertical spread in the points suggests variations in CO_2 concentration, which may arise in (at least) two different ways: it may reflect (1) differences in CO_2 production rates at low temperature within the parent molecular cloud, or (2) formation of CO_2 by energetic processes in the vicinity of YSOs. Models suggest that the composition of the ices in a molecular cloud depends on both physical conditions and evolutionary state (e.g., Ruffle & Herbst 2001; Garrod et al. 2008). Formation of CO_2 is thought to proceed principally via grain surface reactions such as $CO + O \rightarrow CO_2$ and $CO + OH \rightarrow CO_2 + H$. A cloud with relatively high gaseous CO abundance (determined by

[10] The ternary plot provides a more objective analysis than (say) examining the x–y plot of CO/H_2O versus CO_2/H_2O, which effectively assumes that $N(H_2O)$ scales with total ice column and that the ratios of CO and CO_2 to H_2O represent the abundances of these two molecules in the ices. This can lead to confusion between cloud-to-cloud variations and global trends in ice properties: Serpens provides a well-documented example of a cloud where systematic differences occur in the abundance of H_2O relative to other ices in comparison to other clouds (Whittet et al. 2009 and references therein).

gas-phase chemistry) may thus tend to form ices containing more CO_2 (as well as CO) relative to H_2O. Observed differences in CO_2:H_2O concentration in the Serpens and IC 5146 dark clouds compared with Taurus might be explained in this way (Whittet et al. 2009). The onset of star formation enables another route to CO_2: it is well known that exposure of interstellar ice analogs to energetic radiation promotes CO_2 production in the laboratory (e.g., Ioppolo et al. 2009 and references therein).

In order to distinguish between systemic cloud-to-cloud differences in CO_2 production efficiency and production driven by the individual YSOs they contain, it is informative to compare lines of sight within individual clouds. Unfortunately, at present, only Taurus has sufficient coverage for a meaningful comparison: all available data for this region are plotted in the right-hand frame of Figure 10. It is notable that the five YSOs in this sample all lie above the trend for field stars. This vertical separation suggests that each YSO has a significant local component, as well as a molecular-cloud component, to its total dust column, and that CO_2 is being produced in the local component by processes driven by the YSO itself. This effect is seen in both P+NP and P+CIM YSOs, suggesting that energetic CO_2 production is not strongly correlated with the heating responsible for crystallization.

To summarize, it appears that the distribution of points in Figure 10 can be explained by the following.

1. Variation in CO_2 production efficiency that results from differences in the chemistry and/or evolutionary state of the parent molecular cloud.
2. A trend of condensation versus sublimation of CO-rich ices that culminates in crystallization of the ices toward YSOs with the highest degrees of thermal processing.
3. Enhanced CO_2 production by energetic processes in the vicinity of YSOs.

5.4. Correlation with YSO Spectral Index

To provide an evolutionary classification for each YSO, we estimate the spectral index α represented by the mean slope of the spectral energy distribution (SED),

$$\alpha \equiv \frac{d \log \lambda F_\lambda}{d \log \lambda} \approx \frac{\log \lambda_2 F_{\lambda_2} - \log \lambda_1 F_{\lambda_1}}{\log \lambda_2 - \log \lambda_1}, \quad (9)$$

where $\lambda_1 = 2.15$ μm and $\lambda_2 = 25$ μm (e.g., Kenyon & Hartmann 1995). Fluxes are taken from the point-source catalogs of the 2MASS and the *Infrared Astronomical Satellite*, respectively. Values of α for our sources are reported in Table 3. In general, a more positive SED slope (larger α) corresponds to a younger, more deeply embedded YSO with a cool dust envelope and a high column density of molecular-cloud material. As the YSO evolves the envelope dissipates and α is reduced, approaching a value of -3 in the Rayleigh–Jeans limit.

Figure 11 displays plots of α versus $N(H_2O)$, $N(CO_2)$, and the ratio $N(CO_2)/N(H_2O)$. As expected, the individual column densities $N(H_2O)$ and (to a lesser degree) $N(CO_2)$ correlate positively with α, indicating larger ice columns toward more deeply embedded YSOs. These trends are consistent with those found by Zasowski et al. (2009, their Figure 13) for a smaller sample of low-mass YSOs in the Taurus region. The α versus $N(CO_2)/N(H_2O)$ data (lower panel) are uncorrelated or weakly anticorrelated. Several YSOs display CO_2 concentrations in excess of the range occupied by field stars sampling dark clouds (indicated by horizontal dotted lines in the lower panel of Figure 11), a difference that tends to become more pronounced

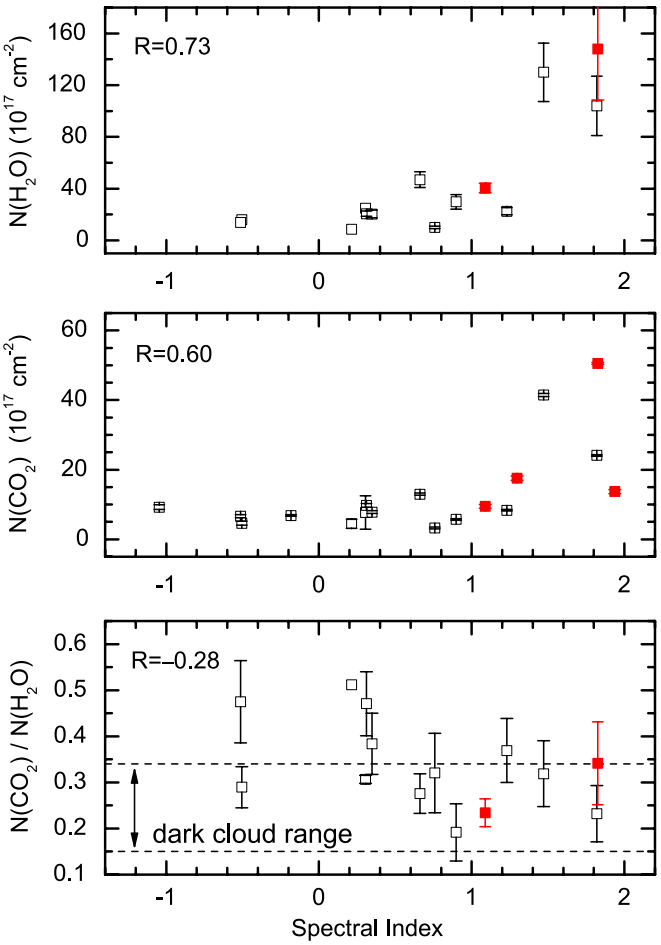

Figure 11. Plots of spectral index vs. CO_2 and H_2O column densities (top and middle frames) and the ratio between them (bottom frame) for YSOs in our sample. Open squares and red squares are P+NP YSOs and P+CIM YSOs, respectively. Horizontal dashed lines in the bottom panel delineate the $N(CO_2)/N(H_2O)$ range observed in field stars toward dark clouds (Taurus, Serpens, and IC5146; Whittet et al. 2007, 2009).

(A color version of this figure is available in the online journal.)

for lower values of α, consistent with a trend toward higher CO_2 abundances in ices toward more evolved YSOs. These results provide further tentative support for enhanced CO_2 production in the environments of some YSOs.

5.5. The Partition of Oxygen between Polar and Nonpolar Ices

Previous observations of background field stars suggest that the abundance of elemental oxygen in the ices in the cold, dense interstellar medium shows consistent behavior from cloud to cloud, and that the distribution of the oxygen between polar and nonpolar components is almost invariant in such regions (Whittet et al. 2009). The extent to which these findings apply to lines of sight toward YSOs is investigated here. Again, we begin by assuming that the three molecules H_2O, CO, and CO_2 represent a nearly complete inventory of oxygen reservoirs in the ices (see Whittet et al. 2007, 2009 for discussion and caveats). The column densities of elemental oxygen sequestered into polar and nonpolar mantles is then given by

$$N(\mathrm{O})_{\mathrm{polar}} = N(\mathrm{H_2O}) + f_1 N(\mathrm{CO}) + 2 f_2 N(\mathrm{CO_2}) \quad (10)$$

$$N(\mathrm{O})_{\mathrm{nonpolar}} = (1 - f_1) N(\mathrm{CO}) + 2(1 - f_2) N(\mathrm{CO_2}), \quad (11)$$

where f_1 and f_2 are the fractions of all solid-phase CO and CO_2 molecules, respectively, in the polar ices. Values of f_1 are

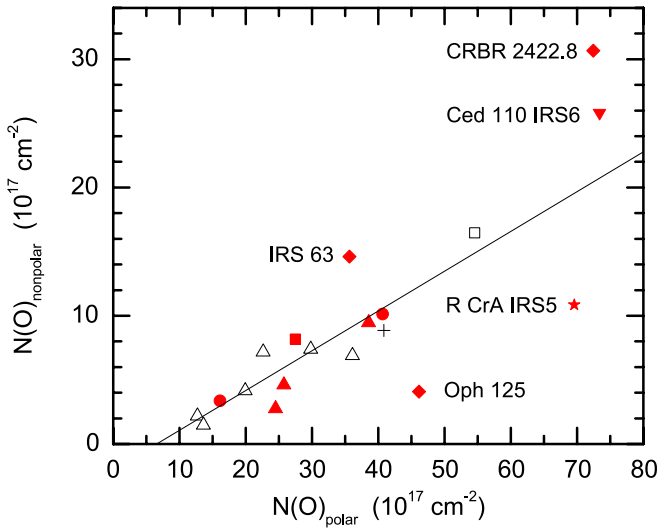

Figure 12. Plot of the estimated column density of elemental oxygen in the polar and nonpolar ices. Black symbols represent field stars from Whittet et al. (2009) in Taurus (triangles), Serpens (square), and IC5146 (plus sign). Red symbols represent YSOs in Taurus (upright triangles), Serpens (square), ρ Oph (diamonds), Perseus (circles), Chameleon (inverted triangle), and CrA (star). The line is the linear least-squares fit to field stars only.

(A color version of this figure is available in the online journal.)

taken from previous work (Chiar et al. 1994, 1995, 2011; Kerr et al. 1993) where $f_1 = 0.17$ for Serpens, 0.12 for Taurus and IC 5146, and 0.19 for ρ Oph; for clouds with no direct measurement, we adopt the Taurus value. The parameter f_2 is evaluated using the χ^2_ν fitting results of the present paper for YSOs and of Whittet et al. (2007, 2009) for field stars. The average values of f_2 are 0.73 for YSOs and 0.85 for field stars.

Figure 12 plots $N(\mathrm{O})_{\mathrm{nonpolar}}$ versus $N(\mathrm{O})_{\mathrm{polar}}$ for YSOs and field stars. The correlation line shown is for field stars only: although YSOs show greater scatter, the majority are nevertheless consistent with the field-star trend. Preferential loss of nonpolar mantles (distribution below the correlation line) is expected in situations where ices are warmed significantly: pure CO, for example, will sublimate at $T > 17$ K. The opposite effect where nonpolar ices tend to dominate (distribution above the correlation line) may arise in the coldest, densest clouds or in situations where gas-phase chemistry favors efficient CO production. These processes might readily explain the loci of certain YSOs. It is notable that three of the most extreme cases lie in the same cloud (ρ Oph: CRBR 2422.8-3423, IRS 63 and Oph 125). This cloud is known to contain relatively steep temperature gradients, from the coldest cores to relatively warm environments subject to a local radiation field enhanced by the presence of nearby luminous stars (Liseau et al. 1999; Di Francesco et al. 2004).

6. CONCLUSIONS

We have reduced and analyzed 10–19.5 μm spectra from the *Spitzer* archive for 28 YSOs exhibiting CO_2 bending-mode ice absorption features, and characterized them by fitting model spectra using data for laboratory analogs with different compositions and temperatures. Modeling leads to classification of the spectra into two groups: P+NP and P+CIM. YSOs in the P+NP group exhibit simple CO_2 absorption profiles resembling those of field stars such as Elias 16, consistent with ices at low temperatures (typically 10–20 K) and dominated by the polar ice component. YSOs in the P+CIM group exhibit structure in the profiles consistent with the presence of ices formed or modified at temperatures substantially higher than those prevailing in cold molecular clouds.

Analyses of data on the abundances of the three principal molecules (H_2O, CO, and CO_2) present in the ices suggests systematic variations in composition determined by initial conditions and/or subsequent evolution. Variations in CO_2 production efficiency resulting from differences in the chemistry and/or evolutionary state of the parent molecular cloud plays a role in determining the abundance of CO_2 in the ices prior to any further evolution in the vicinity of YSOs. The abundance of CO_2 is typically enhanced in lines of sight to YSOs compared with those toward field stars sampling quiescent regions of the prototypical (Taurus) molecular cloud. Thermal or energetic processing driven by the YSOs themselves may thus be responsible for enhanced production of CO_2. Warming causes sublimation of CO from the ices in the lines of sight to many YSOs, a trend that culminates in crystallization of the ices toward those with the highest degrees of thermal processing. The origin of the crystallized ice component remains an important unanswered question: Pontoppidan et al. (2008) propose a distillation process involving the nonpolar ices; our fits suggest a redistribution of CO_2 from polar to crystalline ices toward some YSOs, consistent with thermal processing of the more abundant polar component.

The ternary plot appears to be a valuable analytical tool for studying interstellar ices. To fully exploit its potential, it will be important in the future to obtain reliable data for H_2O, CO, and CO_2 in a greater number of lines of sight, with adequate sampling of both field stars and YSOs in representative molecular clouds and star formation regions covering a range of evolutionary states. The H_2O, CO_2, and CH_3OH system may also be a valuable one to study with this analytical approach, as CO_2 and CH_3OH represent alternative routes for CO chemistry in the environments where H_2O-rich ices form. Again this will require acquisition of new data, specifically to extend the database of CH_3OH detections toward sources with existing data for CO_2.

This work is based on observations made with the *Spitzer Space Telescope*, which is operated by the Jet Propulsion Laboratory, California Institute of Technology, under a contract with NASA. Financial support for this research was provided by the *Spitzer* General Observer and Archival Research Programs (JPL/Caltech Support Agreements nos. 1264149 and 1290823), the NASA Exobiology and Evolutionary Biology program (grant NNX07AK38G), the NASA Astrobiology Institute (grant NNA09DA80A), and the NASA New York Space Grant Consortium. We are grateful to an anonymous referee for helpful comments.

Facilities: Spitzer (IRS), IRTF (SpeX), FLWO:2MASS, CTIO:2MASS

REFERENCES

Bergin, E. A., Melnick, G. J., Gerakines, P. A., Neufeld, D. A., & Whittet, D. C. B. 2005, ApJ, 627, L33
Boogert, A. C. A. 1999, PhD thesis, Univ. Groningen
Boogert, A. C. A., et al. 2004, ApJS, 154, 359
Boogert, A. C. A., et al. 2008, ApJ, 678, 985
Chiar, J. E., Adamson, A. J., Kerr, T. H., & Whittet, D. C. B. 1994, ApJ, 426, 240
Chiar, J. E., Adamson, A. J., Kerr, T. H., & Whittet, D. C. B. 1995, ApJ, 455, 234
Chiar, J. E., et al. 1998, ApJ, 498, 716

Chiar, J. E., et al. 2011, ApJ, in press
Cuppen, H. M., van Dishoeck, E. F., Herbst, E., & Tielens, A. G. G. M. 2009, A&A, 508, 275
Dartois, E., Demyk, K., d'Hendecourt, L., & Ehrenfreund, P. 1999, A&A, 351, 1066
d'Hendecourt, L. B., Allamandola, L. J., Grim, R. J. A., & Greenberg, J. M. 1986, A&A, 158, 119
Di Francesco, J., André, P., & Myers, P. C. 2004, ApJ, 617, 425
Ehrenfreund, P., Boogert, A. C. A., Gerakines, P. A., Tielens, A. G. G. M., & van Dishoeck, E. F. 1997, A&A, 328, 649
Ehrenfreund, P., Dartois, E., Demyk, K., & d'Hendecourt, L. 1998, A&A, 339, L17
Ehrenfreund, P., et al. 1999, A&A, 350, 240
Garrod, R. T., Weaver, S. L. W., & Herbst, E. 2008, ApJ, 682, 283
Gerakines, P. A., Schutte, W. A., Greenberg, J. M., & van Dishoeck, E. F. 1995, A&A, 296, 810
Gerakines, P. A., et al. 1999, ApJ, 522, 357
Gibb, E. L., Whittet, D. C. B., Boogert, A. C. A., & Tielens, A. G. G. M. 2004, ApJS, 151, 35
Gibb, E. L., et al. 2000, ApJ, 536, 347
Herbst, E., & van Dishoeck, E. F. 2009, ARA&A, 47, 427
Houck, J. R., et al. 2004, ApJS, 154, 18
Ioppolo, S., Palumbo, M. E., Baratta, G. A., & Mennella, V. 2009, A&A, 493, 1017
Kenyon, S. J., & Hartmann, L. 1995, ApJS, 101, 117
Kerr, T. H., Adamson, A. J., & Whittet, D. C. B. 1993, MNRAS, 262, 1047
Knez, C., et al. 2005, ApJ, 635, L145
Lamzin, S. A., Melnikov, S. Y., Grankin, K. N., & Ezhkova, O. V. 2001, A&A, 372, 922
Langer, W. D., van Dishoeck, E. F., Bergin, E. A., Blake, G. A., Tielens, A. G. G. M., Velusamy, T., & Whittet, D. C. B. 2000, in Protostars and Planets IV, ed. V. Mannings, A. P. Boss, & S. S. Russell (Tucson, AZ: Univ. Arizona Press), 29
Li, J. Z., Ip, W. H., Chen, W. P., Hu, J. Y., & Wei, J. Y. 2001, ApJ, 549, L89
Liseau, R., et al. 1999, A&A, 344, 342
Martin, P. G., & Whittet, D. C. B. 1990, ApJ, 357, 113
Moore, M. H., Ferrante, R. F., Moore, W. J., & Hudson, R. 2010, ApJS, 191, 96
Nummelin, A., Whittet, D. C. B., Gibb, E. L., Gerakines, P. A., & Chiar, J. E. 2001, ApJ, 558, 185
Oba, Y., Watanabe, N., Kouchi, A., Hama, T., & Pirronello, V. 2010, ApJ, 712, L174
Persi, P., Marenzi, A. R., Gómez, M., & Olofsson, G. 2001, A&A, 376, 907
Pontoppidan, K. M., Dullemond, C. P., van Dishoeck, E. F., Blake, G. A., Boogert, A. C. A., Evans, N. J., Kessler-Silacci, J. E., & Lahuis, F. 2005, ApJ, 622, 463
Pontoppidan, K. M., et al. 2003, A&A, 408, 981
Pontoppidan, K. M., et al. 2008, ApJ, 678, 1005
Ruffle, D. P., & Herbst, E. 2001, MNRAS, 324, 1054
Shenoy, S. S., Whittet, D. C. B., Ives, J. A., & Watson, D. M. 2008, ApJS, 176, 457
Skrutskie, M. F., et al. 2006, AJ, 131, 1163
Tanaka, M., Nagata, T., Sato, S., & Yamamoto, T. 1994, ApJ, 430, 779
Tielens, A. G. G. M., Tokunaga, A. T., Geballe, T. R., & Baas, F. 1991, ApJ, 381, 181
van Broekhuizen, F. A., Groot, I. M. N., Fraser, H. J., van Dishoeck, E. F., & Schlemmer, S. 2006, A&A, 451, 723
Watson, D. M., et al. 2004, ApJS, 154, 391
White, D. W., Gerakines, P. A., Cook, A. M., & Whittet, D. C. B. 2009, ApJS, 180, 182
Whittet, D. C. B., Cook, A. M., Chiar, J. E., Pendleton, Y. J., Shenoy, S. S., & Gerakines, P. A. 2009, ApJ, 695, 94
Whittet, D. C. B., Gerakines, P. A., Hough, J. H., & Shenoy, S. S. 2001, ApJ, 547, 872
Whittet, D. C. B., Shenoy, S. S., Bergin, E. A., Chiar, J. E., Gerakines, P. A., Gibb, E. L., Melnick, G. J., & Neufeld, D. A. 2007, ApJ, 655, 332
Whittet, D. C. B., et al. 1998, ApJ, 498, L159
Zasowski, G., Kemper, F., Watson, D. M., Furlan, E., Bohac, C. J., Hull, C., & Green, J. D. 2009, ApJ, 694, 459